Estimating the Distribution of Snow Water Equivalent and Snow Extent Beneath the Cloud-Cover in the Salt-Verde River Basin, Arizona

N.P. MOLOTCH[1], S.R. FASSNACHT[2], S.R. HELFRICH[3], AND R.C. BALES[1]

ABSTRACT

The temporal and spatial continuity of spatially distributed estimates of snow water equivalent (SWE) and snow-covered area (SCA) is limited by the availability of cloud-free satellite imagery, as SCA is required to define the spatial domain of Snow Telemetry (SNOTEL) point SWE interpolation. In order to extend the continuity of these estimates in time and space to areas beneath the cloud cover, gridded temperature data were used to define the spatial domain of SWE interpolation in the Salt-Verde Watershed of Arizona. An accuracy optimization function of gridded positive accumulated degree-days (ADD) and binary SCA (derived from the Advanced Very High Resolution Radiometer (AVHRR)) was used to define a threshold temperature to define the area capable of having snow cover. The optimized threshold temperature increased during snow accumulation periods, reaching a peak at maximum snow extent. The thresholds then decrease during the first time period after peak snow extent due to the low amount of energy required to melt the "intermittent" snow cover at lower elevations. The area defined as being capable of having snow cover was then used to define the spatial domain of the SWE interpolation. The simulated snow capable area was compared to observed SCA from AVHRR to assess the simulated snow map accuracy. During periods without precipitation, the average commission and omission errors were 12.2% and 8.0% respectively. Commission and omission errors increased to 12.9% and 18.7% during periods of precipitation. The analysis shows that temperature data can be useful in defining the snow extent beneath clouds and therefore improve the spatial and temporal continuity of SCA and SWE products.

Keywords: snow water equivalent, snow cover, time series, temperature, hydrological data

INTRODUCTION

Runoff from the Salt-Verde River Basin is the primary source of locally derived surface water for more than 3 million people in the Phoenix metropolitan area (U.S. Census 2002). In addition to its importance for municipal water use, runoff from the Salt-Verde basin also provides water for agriculture and for hydropower generation. The Roosevelt Dam is the primary water delivery and retention management structure in the basin, providing over 1.6 million-acre feet of storage (Salt

[1] Department of Hydrology and Water Resources, University of Arizona, PO BOX 210011 Tucson, Arizona, 85721-0011, USA.
[2] Departments of Earth Resources and Forest Sciences, Natural Resources Building, Room 335 Colorado State University, Fort Collins, Colorado 80523-1482 USA.
[3] NOAA, National Ice Center, Washington D.C., USA.

River Project, 2002). The complexity of managing the water balance of the Roosevelt Reservoir for municipal, agricultural, hydropower and flood control uses, makes accurate daily forecasts of runoff and potential runoff paramount. Snow water equivalent (SWE) is the primary water storage variable for the calculation of potential runoff during the winter and spring. The intermittent nature of the snow cover in the basin makes daily SWE estimates useful for runoff forecasting.

Daily point measurements of SWE and air temperature are made at Snow Telemetry (SNOTEL) stations across the Western U.S. and are managed by the Natural Resource Conservation Service (NRCS). Carroll and Carroll (1993) have shown that these point measurements can be interpolated to estimate the spatial distribution of SWE. In order to define the spatial domain of the SWE interpolation, estimates of snow-covered area (SCA) are required. The National Weather Service's (NWS) National Operational Hydrologic Remote Sensing Center produces daily binary (snow or no snow) SCA maps at a 1-km^2 resolution for the Western U.S. using both the AVHRR and GOES satellites (Carroll *et al.*, 2001), however the SCA data are extracted using visible and near infrared bands that cannot see through clouds. When clouds are present the use of models to estimate the extent of the snow cover becomes attractive.

Liston (1999) showed that energy and mass balance modeling of the snowpack can be used to estimate the depletion of SCA. If the initial SWE and the snowmelt rate of each pixel is known, the SCA can be calculated by assuming that the SCA of each pixel will become zero when the sum of the daily melt fluxes equals or exceeds the initial SWE of the pixel. The melt rate can be calculated using energy balance calculations that incorporate the net radiation, sensible and latent heat fluxes occurring at the snow/atmosphere interface (Cline *et al.*, 1998; Liston, 1999; Colee, 2000). Calculating the melt rate using physically based energy balance calculations requires measurements (or modeled estimates) of the net radiation and turbulent fluxes, limiting the application of these techniques to areas where these measurements are made. Estimating melt rates in this manner also limits the scale of the application due to the increase in the uncertainty in the input variables as the scale of the application increases (Blöschl, 1999).

Given the scale of this application (35,100 km^2) it is more attractive to pursue a parameter-based approach to estimating melt rates. As a sole index variable, air temperature is most capable of representing snowmelt rates (Zuzel and Cox, 1975) and has been used as an index variable to estimate snowmelt runoff (Rango and Martinec, 1982), residual SWE (Ferguson, 1984) and the depletion rate of SCA (Anderson, 1974; Dunne and Leopold, 1978; Ferguson 1984, 1986; Buttle and McDonnell, 1987). Rango and Martinec (1982) showed that for a test year, real-time estimates of maximum SWE can be obtained as follows: an initial guess of SWE is made and a corresponding historical depletion curve chosen; if the plot of SCA versus the temperature index does not match the chosen curve, a new curve is selected and the initial guess of SWE is updated. This approach became the basis for the snowmelt runoff model (SRM) in which forecasts of runoff can be obtained by using the SWE estimates and predictions of the temperature index. The technique has been used to model snowmelt runoff in the Himalaya (Kumar *et al.*, 1991), in the Rhein-Felsberg of Switzerland (Baumgartner *et al.*, 1986), in the Cordevole River Basin of the Italian Alps (Swamy *et al.*, 1997), in the Rio Grande of Colorado (Rango, 1988), and in other locations.

In this research point daily SNOTEL and U.S. Cooperative Observer (COOP) measurements of air temperature are spatially distributed and summed to derive gridded accumulated degree-day (ADD) index maps. The ADD index is used in conjuncture with remotely sensed SCA to define the threshold temperature at the "snow-line". The main assumption is that, at the perimeter of the snow extent, cloud-covered pixels, with a specific ADD value have the same initial SWE and the same snowmelt rate, and therefore become snow-free, at the same ADD value as cloud-free pixels. The basis for using the ADD index grid to define the spatial domain of the SWE interpolation is based on the relationship between SWE and snowmelt flux:

$$SWE_{i+1} = SWE_i - M,$$

where M is the melt flux, SWE_{i+1} is the residual SWE after time step i and SWE_i is the initial SWE of the pixel. When SWE is equal to zero, SCA is equal to zero and therefore setting SWE_{i+1} equal to zero in the expression above, shows that when the melt flux, M, is equal to the initial snow water equivalent, SWE_i, the snow-covered area is equal to 0. When bare ground can be observed from AVHRR then the melt flux, M, required to melt SWE_i can be determined by summing the melt flux, M, up to the date when SCA is 0. Cloud-covered pixels with the same initial SWE_i as cloud-free pixels will become snow-free at the same melt flux, M. The melt flux, M, can be expressed as:

$$M = a * ADD,$$

where a is equal to the degree-day coefficient (cm day^{-1} $^{\circ}C^{-1}$), and ADD ($^{\circ}C$) is equal to the accumulated degree-day index. Thus, the ADD value of snow-free pixels in cloud-free areas can be used to determine if there is snow in cloud-covered areas.

STUDY AREA

The Salt-Verde River Basin is located within the Lower Colorado Basin in east-central Arizona of the southwestern U.S. (Figure 1). The drainage area is 35,100 km^2, and has an elevation range of 280-3850 m. Streamflow in the Salt-Verde River Basin is regulated by a number of control structures, including the Roosevelt and Horseshoe Reservoirs. Thirty nine percent of the annual precipitation, recorded at SNOTEL stations within the basin, falls as snowfall (Serreze *et al.*, 1999). The vegetation varies from desert scrub in the lower regions through Pinyon Juniper in the mid-elevations through to Ponderosa Pine and Fir-Spruce in the higher elevations.

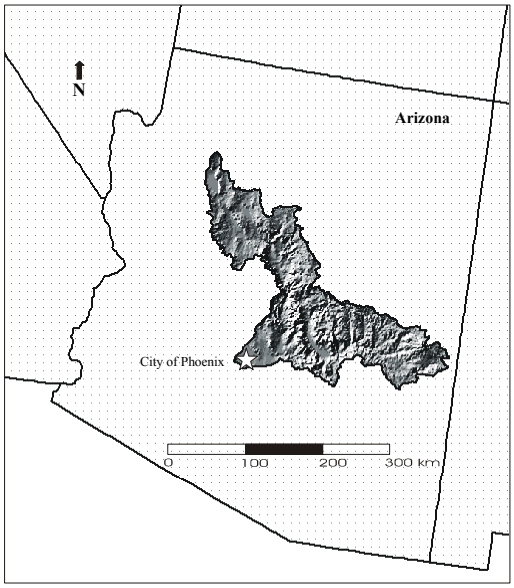

Figure 1. Hillshade relief of the Salt-Verde River Basin, Arizona.

STUDY PERIOD

The spatial distribution of SCA is used in the derivation of total SWE. Clouds hamper the ability to determine if an area has snow cover, and thus clouds inhibit the ability to determine the quantity of SWE stored in the basin. Figure 2a displays the area of cloud-covered pixels within areas of the

Salt-Verde Basin that had snow cover during the series, i.e., the annual maximum snow extent. These cloud-covered pixels represent the area of undeterminable SCA and SWE, for selected dates. These are limited to annual maximum snow extent to avoid overestimation of undetermined pixels in the Salt-Verde Basin. Figure 2b shows the binary SCA over the same dates. These are derived from those areas not obscured by clouds. Clouds were present intermittently throughout the study period (Figure 3). During these intervals, there are underestimates of SCA. Figure 2b suggests that SCA was depleting until early February when a snow event increased the SCA. The SCA decreased between the March 9th and the March 25th observations and increased between the March 25th and March 31st observations (Figure 2b, 3). This was followed by a sharp decrease in SCA for the remainder of the season. The product of binary SCA and the interpolated SWE is the total SWE (Figure 2c). This is restricted to cloud-free areas. This curve follows the same pattern as the SCA, with the exception of the March 9th observation, where the total SWE increased while the SCA decreased. The average SNOTEL SWE doubled during that period (Figure 2d).

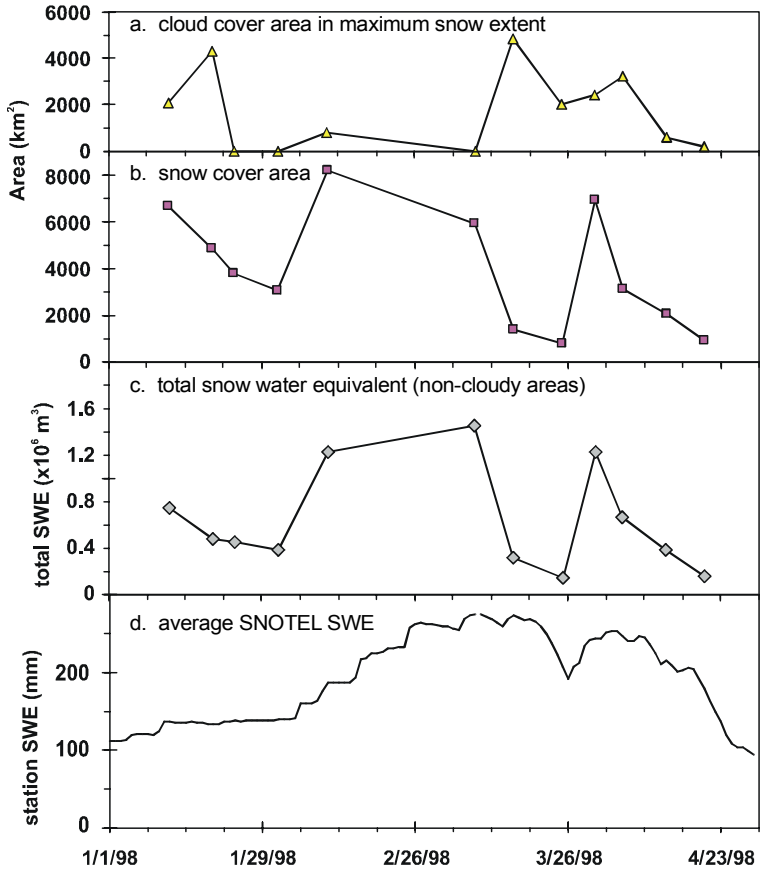

Figure 2. Summary of the Salt-Verde Basin 1998 snow-related imagery and SNOTEL data.

METHODS

The SCA and interpolated SWE datasets were developed by the National Aeronautics and Space Administration's Southwest Regional Earth Science Application Center (SW RESAC 2002a, b). These datasets and a new temperature dataset, developed for this project, were compared and combined to investigate the capability of gridded temperature to estimate the extent of snow cover.

SWE Time Series

Daily spatially distributed SWE estimates at 1-km^2 resolution were estimated by interpolating point SWE measurements from SNOTEL stations using the methods of Fassnacht *et al,.* (*in submission*). For each grid cell in the basin, all SNOTEL sites within a 200-km radius, including those outside of the basin, were identified. A linear regression was computed between elevation and SWE for all of the SNOTEL sites within the search radius. This hypsometric relationship was used to estimate SWE for each grid cell using a 1-km digital elevation model (DEM). A residual was obtained at each grid block where an observing SNOTEL station was located by removing the observed value from the analysis (i.e. jack-knifing) and subtracting the observed SWE from the computed SWE. In order to remove any elevation dependent bias in the residuals, the residuals were regressed to a datum of 5000 m.a.s.l. using the following expression:

$$R_L = R * L * (D - E),$$

where R_L (m) is equal to the lapsed residual, R (m) is equal to the residual, L is equal to the lapse rate (9.8 m/1000m), D (m) is equal to the datum of 5000 m and E (m) is equal to the elevation. The lapse rate used was chosen for simplicity, as it was the lapse rate used for regressing the temperature residuals (the dry adiabatic lapse rate of 9.8 ºC/km). Once regressed to the common datum, the lapsed residuals were spatially distributed using inverse distance weighting with a polynomial of 2. The gridded residual surface was regressed back to the basin surface using the same lapse rate and subtracted from the hypsometrically derived SWE grid in order to derive the final SWE surface. Daly *et al.* (2000) used the same method, except one hypsometric relationship was computed for each sub-basin instead of using a moving search radius to compute the hypsometric relationship at each pixel. The interpolated SWE grids have units of millimeters of water.

SCA Imagery

Fractional SCA was determined from NOAA-AVHRR imagery using the methods of Rosenthal (1996). Fractional SCA was generated with a spectral mixture analysis of AVHRR imagery received by the University of California at Santa Barbara. Images were georegistered and calibrated using various reference images, as outlined in Daly *et al.* (2000). Radiance values were atmospherically corrected using the techniques describe by Vermote *et al.* (1997). A 1.1-km^2 band resolution is obtainable from the AVHRR and resampled to 1-km^2. Surface reflectance values were derived for channel 1 (0.58 to 0.68 μm) and channel 2 (0.72 to 1.10 μm) using techniques described by Rosenthal (1996). The surface reflectance in channel 3 (3.55 to 3.93 μm) measurements was separated from the emittance component in the same band range with the aid of channel 4 (10.3 to 11.3 μm) measurements. Channel 4 measurements were also used in the derivation of brightness temperatures for the image. Clouds often contain similar reflective and brightness temperature characteristics to those of snow. Cloud masks were generated by an image analysis using techniques described in Simpson *et al.* (1998) to eliminate those pixels determined to be clouds rather than snow. This technique required manual interpretation and editing of pixels. Water and highly reflective land features were also masked to prevent interpretation as snow. Brightness temperatures were used to further discriminate pixels with the potential of containing SCA from those without such potential (Rosenthal, 1996). Derived surface reflectance and brightness temperatures were used as input to a binary decision tree algorithm to determine which pixels are likely to contain snow-cover. Pixels determined to contain snow-cover were then processed using a regression heuristic to estimate the snow-covered fraction within the pixel.

The focus of this research is to define the spatial domain of the point SWE interpolation beneath the cloud cover and therefore fractional SCA estimates were unnecessary. Furthermore, validation of fractional SCA is difficult in cloud-free areas, much less, in areas under the cloud cover. Therefore, the fractional SCA grids were resampled to binary SCA based on the condition that any detectable amount of SCA (SCA > 0%) is a snow-covered pixel and assigned a value of 1, with all other cloud-free pixels assigned a value of 0 (Figure 3).

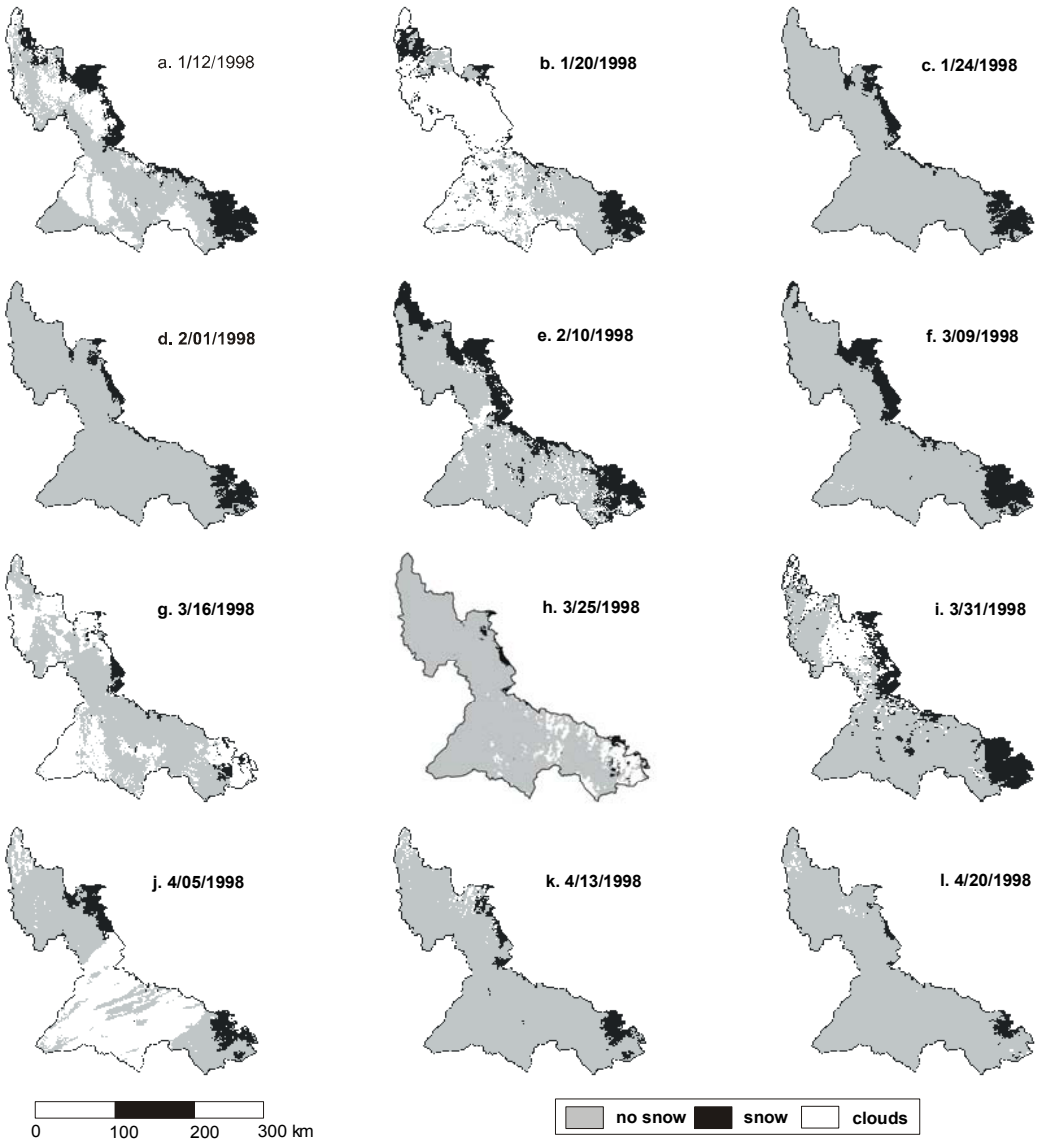

Figure 3. Binary snow-covered area time series derived from AVHRR for the Salt-Verde watershed, 1998.

Gridded Temperature Data

Point temperature data were interpolated for the basin using the same method used to generate the gridded SWE time series maps. Daily average temperatures were measured at 231 SNOTEL sites and daily maximum and minimum temperatures were measured at 668 COOP sites. The COOP network is administered by the National Weather Service, and the data are archived by the

National Climatic Data Center. For the COOP sites, mean daily temperatures were estimated by averaging the daily maximum and minimum temperatures. Daily average temperature maps were generated on a 1-km^2 grid in tenths of degrees Celsius. The ADD index used in this analysis is a summation of the average daily temperatures above 0º C. It is expressed as:

$$ADD = \sum \max[T_a, 0]$$

Where T_a is equal to the average daily temperature of the grid cell.

Temperature Threshold Estimation

For each day for which AVHRR derived SCA was available, an accumulated degree-day grid was generated from average daily temperature grids across the Salt-Verde Watershed. Summing the positive daily average temperatures observed during the 7 days preceding the AVHRR acquisition generated the accumulated degree-day grids. In order to assess the impact of the number of days used in the summation, ADD grids were also generated using temperature data from the 3, 5, 9, and 11 days preceding the AVHRR acquisition (Figure 4).

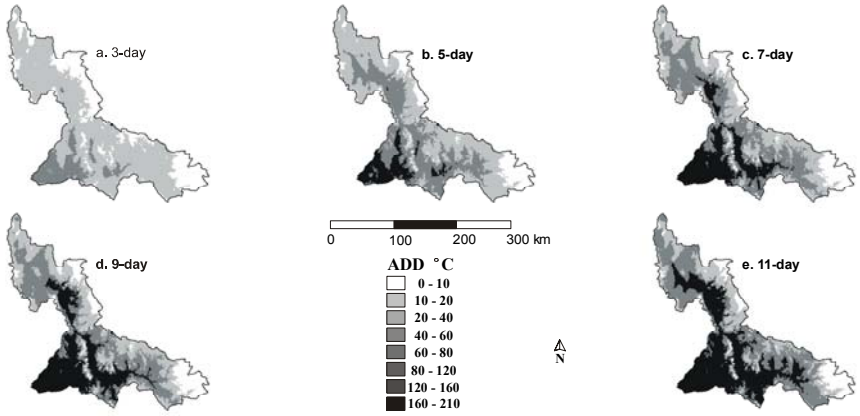

Figure 4. Accumulated degree-day grids for March 16, 1998.

As shown in Figure 5, in 11 of the 12 days, the fraction of pixels observed as snow by AVHRR that were identified by the ADD temperature mask reaches unity at thresholds at or well below the ADD value of 75 ºC. Therefore, the accumulated degree-day grids were converted to binary grids based on a threshold number of ADDs, ranging from 1ºC - 75ºC at 1ºC increments. A geographic information system (GIS) was used to resample each ADD grid using the range of threshold values from 1ºC - 75ºC. Pixels were defined as being within the snow capable area if the accumulated degree-day value of the pixel was below the threshold temperature, i.e., from 1ºC to 75ºC. In order to determine the appropriate ADD threshold, the snow capable area grids (as defined by each integer threshold value from 1ºC - 75ºC) were masked to cloud-free areas and compared to the AVHRR-derived SCA grids. Thus, the appropriate ADD threshold value is obtained by training the threshold value in cloud-free areas. The application of this threshold value to areas beneath the cloud-cover is possible under the assumption that the relationship between the snow cover and ADD is the same in cloud-free and cloud-covered areas. Given the relatively short time scale of the cloud-cover with respect to the 7 day accumulation of degree days, it is reasonable to assume that the 7-day ADD threshold acts as an index variable that describes the meteorological conditions over a period of time (i.e. 7-days) that exceeds the influence of relatively short time scale factors such as cloud cover. Additionally, training the threshold value is not possible in cloud-covered areas due to the lack of information about the snow cover beneath the clouds. Four conditions were incorporated into the GIS analysis to compare the SCA and snow capable area grids: 1) an accurate commission, where both AVHRR-derived SCA and snow

capable area indicate snow, 2) an error of omission, where AVHRR-derived SCA indicates snow but the snow capable area indicates no snow, 3) an error of commission, where AVHRR-derived SCA indicates no snow whereas the snow capable area indicates the presence of snow, and 4) an accurate omission, where both AVHRR-derived SCA and snow capable area indicate no snow present. Once the appropriate ADD threshold was selected for each simulation, the snow capable area grids and SCA grids were used to define the spatial domain of the point SWE interpolation.

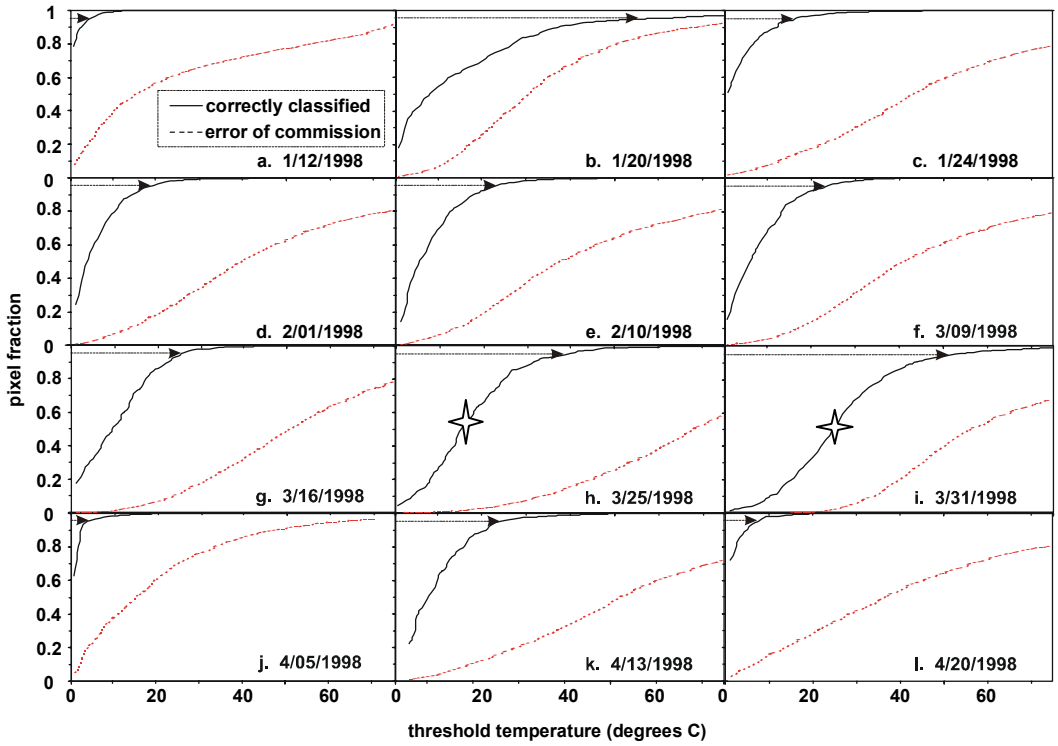

Figure 5. Threshold accumulated degree-day temperature versus the correctly classified pixel fraction and the error of commission pixel fraction. Arrows indicate the correctly classified pixel fraction equal to 95% or *T(95%)*. Stars indicate inflection points.

Using the four conditions described above, three techniques were developed to define the threshold temperature that most accurately defined snow extent:

1) T(95%) technique: This technique is defined as the threshold temperature at which the correctly classified pixel fraction equalled 95% (Figure 5). The correctly classified pixel fraction was computed as the ratio of the number of pixels that were accurately simulated as snow-covered to the total number of pixels observed as snow-covered by AVHRR. This technique does not take account of any error of commission.

2) T(max diff) technique: The *T(max diff)* technique accounts for error of commission by defining an error of commission pixel fraction, i.e., the ratio of the number of erroneously committed pixels to the total number of non-snow-covered AVHRR pixels (Figure 5). Both pixel fraction indexes have positive slopes. The slopes of these two lines are not equal and therefore a threshold temperature can be defined that minimizes the error of commission pixel fraction while maximizing the correctly classified pixel fraction (Figure 6). The *T(max diff)* technique defines this threshold temperature as the maximum difference between the correctly classified pixel fraction and the error of commission pixel fraction.

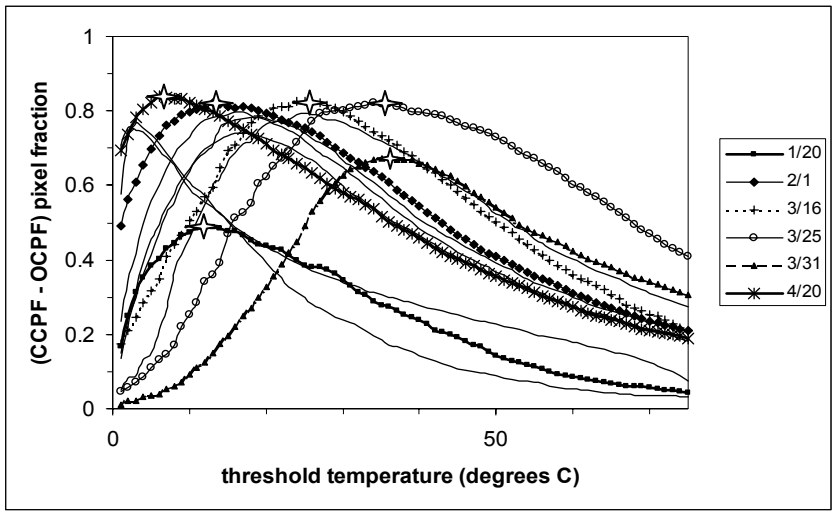

Figure 6. Temperature threshold versus the difference between correctly classified pixel fraction (CCPF) and the error of commission pixel fraction (OCPF). Stars show location of the maximum difference between the two pixel fractions for three of the dates.

3) T(SWE) technique: Both of the above techniques train the threshold temperature based on the cloud-free observations of SCA and do not include information about the SWE. Given that the goal of the techniques is to define the spatial domain of the SWE interpolation it is important to account for the error in SWE estimates caused by both the error of commission and error of omission of pixels. Error of commission causes the SWE interpolation to extend into areas where no snow exists, and error of omission does not extend the SWE interpolation into areas where snow exists. The SWE of the areas erroneously included and excluded from the interpolation may not be equal. This inequality results in errors in the SWE estimates across the domain. The *T(SWE)* technique defines the threshold temperature as the ADD threshold value that results in the most accurate estimate of SWE. This ADD threshold was obtained as follows: estimates of SWE in cloud-free areas were generated using all integer values of ADD from 1ºC - 75ºC to define the spatial domain of the SWE interpolation (Figure 7); a baseline total SWE was generated using the binary AVHRR-derived SCA to define the spatial domain of the SWE interpolation; the ADD threshold value that resulted in the most agreement between the two SWE estimates was selected.

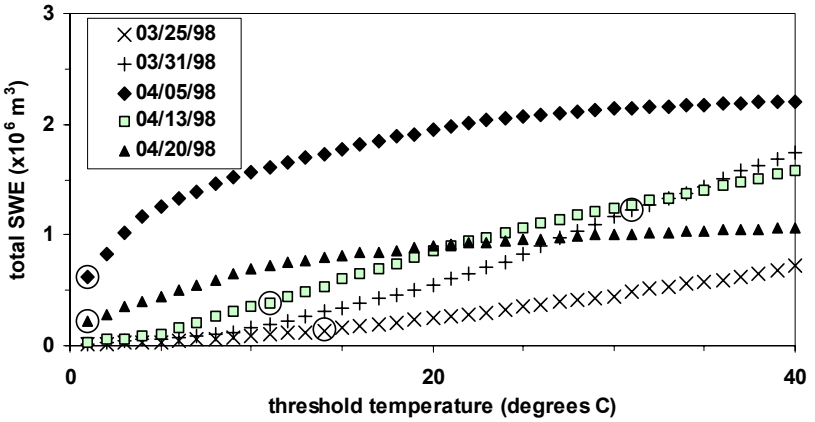

Figure 7. Variation of total SWE with threshold temperature and correlation to AVHRR SCA-derived SWE. The total SWE values obtained when the AVHRR-derived SCA was used to define the spatial domain of the SWE interpolation are shown with circles.

Given that the goal of this research is to improve estimates of SWE under the cloud cover, the *T(95%)* and the *T(max diff)* temperature thresholds were regressed against the *T(SWE)* threshold temperature in order to calibrate the simulated threshold temperatures. The temperature threshold obtained using the *T(max diff)* technique showed the most agreement with the *T(SWE)* technique (Figure 8) and was selected as the preferred method for defining the spatial domain of the SWE interpolation.

The estimates of SWE obtained using the *T(max diff)* to define the spatial domain of the SWE interpolation were evaluated by comparing the estimates with the baseline SWE estimates described above. In this comparison cloud-covered areas were not included so that the total SWE from the *T(max diff)* simulation could be compared to the baseline technique, which used satellite-derived SCA and therefore did not include cloud-covered areas. The product of the mean pixel interpolated SWE and the number of cloud-free pixels was used to compare the *T(max diff)* simulated SWE and the AVHRR-SCA derived SWE. Total basin-wide SWE, including cloud-covered areas, was then simulated using the *T(max diff)* technique to define the spatial domain of the SWE interpolation. This basin-wide simulated SWE was graphically compared to the cloud-free *T(max diff)* simulated SWE and the AVHRR-SCA derived SWE.

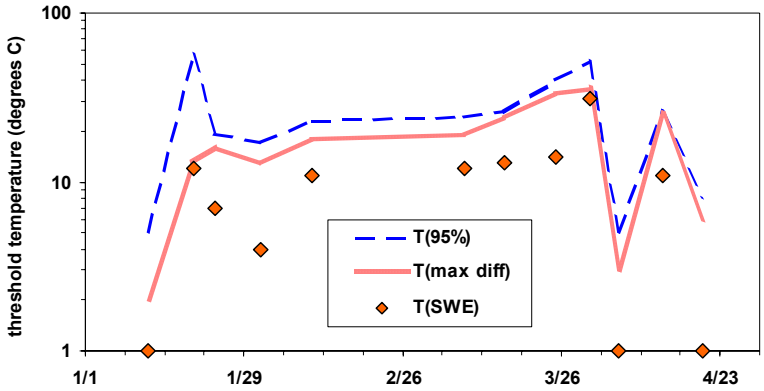

Figure 8. Temporal variation in the different distinctions of the threshold temperature value.

RESULTS

A relationship exists between the accumulated degree-day threshold and the correctly classified pixel fraction (Figure 5a-l); as the threshold temperature is increased, the temperature mask identifies more pixels with observed snow cover from AVHRR. The slope of the relationship decreases dramatically, in all but one simulation (Figure 5b), as the correctly classified pixel fraction approaches unity. In two cases (Figure 5h,i) the correctly classified pixel fraction increases rapidly to an inflection point and then the rate of increase decreases and finally the pixel coverage becomes asymptotic as the correctly classified pixel fraction approaches unity. The error of commission pixel fraction also increases as the ADD threshold increases but at a slower rate (Figure 5). The difference between the two curves on Figure 5a-l was plotted against the threshold temperature (Figure 6). From the curves in Figure 6, an accuracy optimization function was defined that maximized the correctly classified pixel fraction while minimizing the error of commission pixel fraction. The maxima of each curve occurred at a threshold temperature greater than 1^{o}C (Figure 6). The slopes of the rising limbs of the curves are steeper than the falling limbs, with some of the curves resembling a log-normal distribution. The maximum difference is in the range of 0.8 for all dates except for January 20th, with a peak of 0.48, and March 31st with peak at 0.67. Snow cover existed at the lower elevations of the watershed and clouds limited observations of the snow cover at the higher elevations on these dates (Figure 3b,i). The highest maxima for the twelve *T(max diff)* simulations occurred on February 1st, March 16th, March 25th and April 20th

(Figure 6). The snow cover was restricted to the higher elevations of the watershed during these four dates (Figure 3d,g,h,l). Given that the temperature data interpolation was based on hypsometry it is intuitive that the highest maxima occurred on dates where the snow cover exhibited an elevational "snow-line".

Increasing the number of days used in the summation of daily average temperatures to determine the ADD index resulted in a decrease in the slope of the functional relationship between the threshold temperature and the correctly classified pixel fraction (Figure 9a-l). The slope of this relationship for the 3,5,7,9 and 11-day ADD grids was most variable for the 3/31/98 simulation (Figure 9i) and least variable for 2/1/98 and the 4/13/98 simulations (Figure 9d,k, 10).

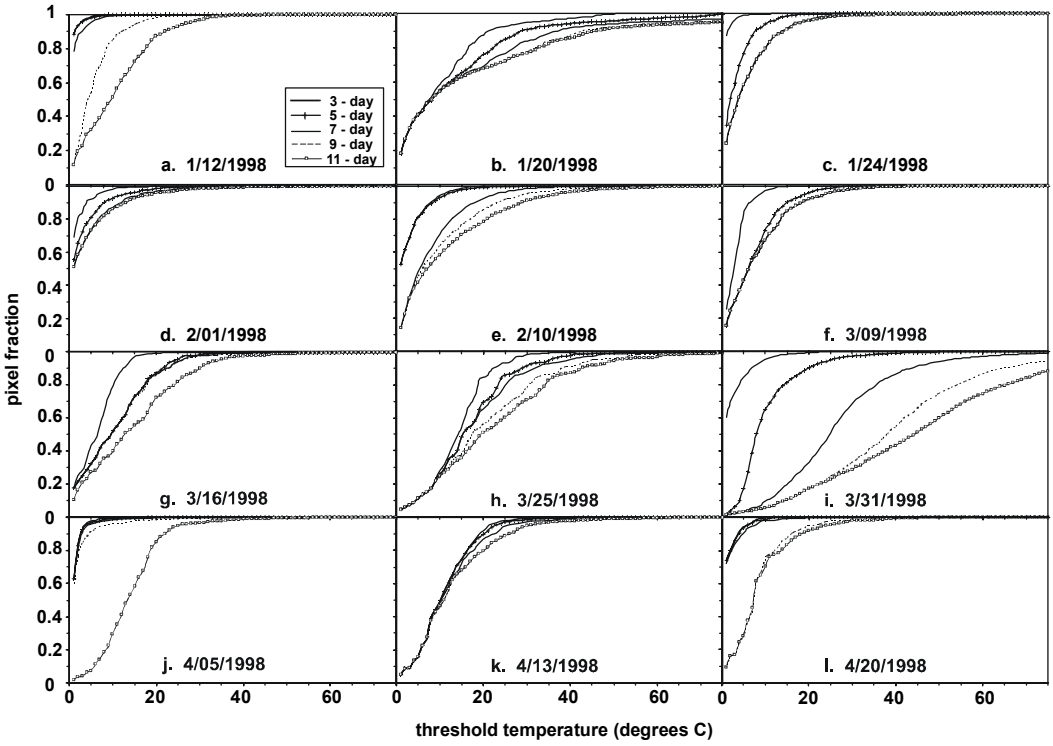

Figure 9. Sensitivity of the correctly classified pixel fraction to the number of days used in the summation of the accumulated degree-day index.

The *T(max diff)* optimized threshold temperature varied with the number of accumulated degree-days (Figure 10). Sensitivity of the maximum difference (Figure 10) matches the sensitivity to the correctly classified pixel plots (Figure 9a-l). The variability in the *T(max)* threshold temperatures was highest for simulation dates where the average daily temperature during the preceding 11 days was above 0 ˚C. Daily average temperatures above 0 ˚C cause the ADD index to increase. The greater the temperature, the larger the increase in ADD index and therefore greater differences between ADD grids summed over different time periods, i.e., 3,5,7,9 or 11 days.

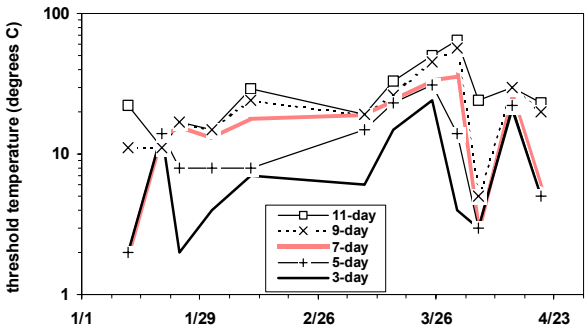

Figure 10. Variation in the threshold temperature derived from the maximum difference between the correctly classified pixel fraction and the error of commission pixel fraction.

The map accuracy of the *T(max diff)* technique is shown in Table 1. Omission errors ranged from 5.3% to 39.5% and commission errors ranged from 9.6% to 15.4%.

The relationship between total SWE volume and threshold temperature is shown for five of the 12 simulations in Figure 7. The total SWE values were calculated from cloud-free pixels only so that they could be compared to the total SWE obtained using the satellite-derived SCA. For the 12 simulations, the threshold temperature required for the total temperature-masked SWE to equal the total satellite-derived total SWE averaged 9.83 and ranged from 1-31 (figure 8), with a standard deviation of 8.33.

A comparison of the different methods to derive the threshold temperature showed that the *T(max diff)* technique came closest to the *T(SWE)* technique, i.e., the baseline threshold temperature (Figure 8). The *T(95%)* technique resulted the highest threshold temperature. The coefficient of determination was 0.75 between the threshold temperatures for the baseline case (i.e., *T(SWE))* and the threshold temperatures derived from the *T(max diff)* technique, with a slope of 1.26 (Figure 11).

Table 1. Average omission (OE) and commission errors (CE) for the 12 simulations.

	No Storm		Storm	
	OE %	CE %	OE %	CE %
T (95%)	4.4	17.8	4.8	41.7
T (max diff)	8.0	12.2	18.7	12.9
T (max diff) regressed	10.6	14.6	15.5	19.0
T (SWE)	35.2	4.1	33.4	6.7

Note: Storm period simulations are shown separately from non-storm periods.

The total SWE volumes generated using the *T(max diff)* technique and the *T(SWE)* technique (i.e. the baseline technique), to define the spatial domain of the SWE interpolation are shown in Figure 12. Baseline total SWE volumes for the 12 simulations ranged from 0.16-1.46 x 10^6 m^3 with a mean of 0.64 x 10^6 m^3 and a standard deviation of 0.44 x 10^6 m^3. Simulated SWE volumes using the *T(max diff)* technique with the regressed calibration showed a mean error of 55% when compared with the *T(SWE)* technique over cloud-free areas only. The total basin-wide simulated SWE, including cloud-covered areas, averaged 1.38 x 10^6 m^3 or 116% greater then the average baseline SWE (i.e. the SWE estimates in cloud-free areas). Baseline total SWE accumulation/ablation patterns appear to be separated into three different peaks with an initial ablation period in January, an accumulation period in February and early March, followed by an

intense ablation period (Figure 12). Accumulation resumed in mid-March resulting in a simulated SWE peak on March 31.

DISCUSSION

In order to assess trends in the functional relationship between threshold temperature and SCA, the time series can be classified into three different accumulation/ablation seasons based on periods of time when SCA increased to a maximum and then decreased to a minimum before increasing again (Figure 2b). The time period from March 25 to April 20 was used to show the relationship between threshold temperature and SWE (Figure 7). The variability in the threshold temperature can be explained by comparing the AVHRR-derived SCA scenes during that time period. On March 16, the snow cover was isolated to the higher elevation areas of the watershed and on slopes with low exposure to solar radiation. The snow cover decreased only slightly from March 16 to March 25 (Figure 3g,h) although a large threshold temperature was required on the 25th to define the area capable of having snow cover. The large threshold can be explained by the fact that larger amounts of energy are needed to melt snow-covered areas that persist throughout the snow melt season. These "seasonal" snow-covered areas tend to have larger amounts of snow and therefore have a more pronounced cold content then the "intermittent" snow-covered areas at lower elevations and on southerly exposures. This phenomenon is intuitive given the ebb and flow of snow cover that occurs in between storm cycles at lower elevations. After March 25 the snow cover increased, reaching a maximum on March 31 (Figure 3h,i). On this date, a threshold temperature of 31^{o} C was required to define the snow capable area. Given that the recent storm had extended the snow cover into the lower elevations a large temperature threshold was required to extend the snow capable area to the lower elevations. The transition from the high threshold temperature of 31^{o} C to the low threshold of 1^{o} C on April 5 is of interest as it reinforces the point that only a small amount of energy is needed to melt the "intermittent" snow cover at lower elevations. After the "intermittent" snow cover had melted, the ADD threshold increased again as more energy was required to melt the "seasonal" snow cover.

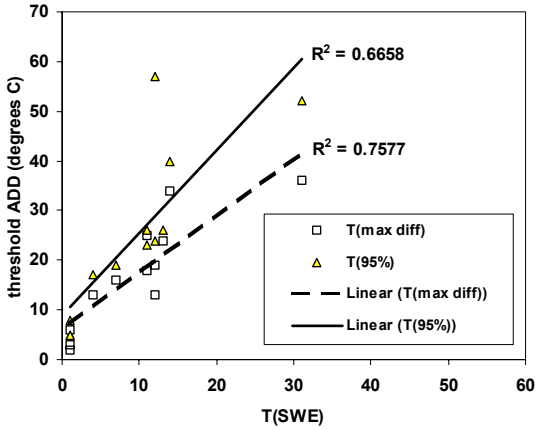

Figure 11. Linear regression of the T(SWE) ADD threshold values (independent variable) and the T(max diff) and T(95%) ADD threshold values (dependent variables).

The difference between the *T(max diff)* technique and the *T(SWE)* technique results in an overestimation of the snow capable area and therefore overestimates of total SWE. However, the total SWE was improved using the calibration of the threshold temperatures from the regression of the *T(SWE)* and *T(max diff)*. The lagged response of the *T(max diff)* temperature threshold peaks (Figure 8) was due to the fact that the functional relationship between the correctly classified pixel fraction and threshold temperature reaches an asymptote while the slope of the functional

relationship for the error of commission pixel fraction was still increasing (Figure 5a-l). This is due to the fact that colder areas (i.e. higher elevations) of the watershed are more likely to have snow cover than warmer areas (i.e. lower elevations).

The commission and omission errors shown in table 1 compare well with more complex models for inference of snow under clouds. Cline and Carroll (1999) used a full energy balance snow cover depletion model to infer the presence of snow under clouds, in which hourly gridded inputs of air temperature, relative humidity, wind speed, incident shortwave and longwave radiation were all required. The model applied here only required daily average temperature data and observations of SCA.

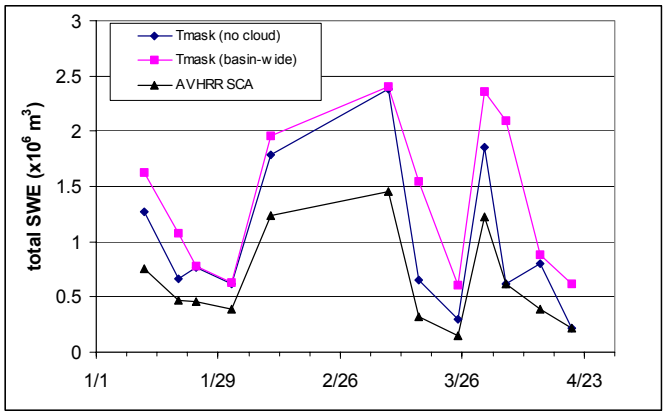

Figure 12. Total SWE estimates masked for the Salt-Verde Basin.

The difference between the basin-wide total SWE and the total SWE calculated for cloud-free areas was greatest on March 16th and 25th (Figure 12). On these two dates cloud cover over the higher elevations limited the observation of snow cover from satellite (Figure 3g,h).

One of the underlying objectives was to achieve a method that could map spatially continuous SWE under clouds. Related to this is the elimination of erroneous SCA pixels that are actually cloud. The differentiation between cloud and snow is difficult because their spectral reflectance signatures are similar in the visible and near-infrared wavelengths. Use of the ADD temperature masks for identifying snow-covered pixels can assist both estimation of snow under clouds and removal of cloud pixels classified as snow. The SWE was mapped under clouds, however the improvement was not quantified because of the difficulty of validating the distribution of SWE at the scale of this application.

There are problems with the SWE maps, especially related to the representativeness of the SNOTEL data (Molotch *et al.*, 2001). However, the SNOTEL network still provides the best measure of ground based SWE distributions. Fassnacht *et al.* (*in submission*) illustrated that the elevation detrended (hypsometric with inverse weighted distance gridding of the residuals) provided the best interpolation method over the study area, they stated that more advanced techniques needed to be investigated.

In order to map SCA beneath clouds in real time during periods of snow accumulation, incorporation of ground and/or satellite measurements of precipitation may be necessary. Applying this analysis to watersheds or time periods with a more pronounced accumulation/ablation season may provide a good comparison to assess the applicability of the methodology to more diverse climatic regimes. The temperature datum used as the reference for the accumulated degree-days should be optimized.

CONCLUSIONS

The primary objective of this research was to determine if gridded daily temperature could be used to define the spatial domain of the SWE interpolation beneath clouds in order to improve the spatial and temporal continuity of gridded SCA and SWE products. Results showed that a relationship exists between the accumulated degree-day temperature data and the snow cover area determined by the AVHRR imagery. Increasing the number of days used to determine the ADD increases the threshold temperature for the index of correct-classification, with stronger response later in the melt season. Accumulated degree-day thresholds increased during snow accumulation periods, reaching a maximum at peak snow extent. The thresholds decrease dramatically during the first time period after peak snow extent due to the low amount of energy required to melt the "intermittent" snow cover at lower elevations. Commission and omission errors for the 12 simulations averaged 12.4% and 11.6% respectively. Errors decreased to 12.2% and 8.0% respectively during non-storm periods. These errors compare well against the results of more complex model simulations. Errors in the spatial domain definition resulted in errors in the SWE estimates. Simulated SWE volumes using the *T(max diff)* technique with the regressed calibration showed a mean error of 55%. The basin-wide total SWE averaged 1.38 x 10^6 m^3 or 116% greater then the average baseline SWE. The difference between the simulated basin-wide SWE and the baseline SWE was greatest on cloudy dates. Simulated SWE volumes show that temperature data can be useful in defining the snow extent beneath clouds and therefore improve the spatial and temporal continuity of SCA and SWE products.

ACKNOWLEDGEMENTS

This research was supported by the NASA Earth Observation System Southwest Regional Earth Science Applications Center <*http://resac.hwr.arizona*>, (NASA grant NAG990005). Additional funding was provided by the NSF Sustainability of semi-Arid Hydrology and Riparian Areas (SAHRA) Science and Technology Center (NSF EAR9876800), HyDIS project (NASA grant NAG5-8503), and the NASA-Raytheon Synergy Program (NASA grant NAG-3006 Subcontract 300623). Data were provided by the Natural Resources Conservation Service of the USDA, through the Western Regional Climate Center and the National Weather Service US Cooperative Observer network, through the National Climatic Data Center. Quality controlled SNOTEL data were obtained from Dr. M.P. Clark at CIRES, University of Colorado, Boulder. Thanks are due to E.B. Halper, D.J. Lampkin and D.A. Wilson for their assistance. Dr. B. Imam was instrumental in providing support in various forms, and his efforts are acknowledged with thanks. Technical support was also provided by K.A. Dressler.

REFERENCES

Anderson, E.A., Conceptual streamflow forecasting model applied to northern New England rivers, *Proceedings of the 31st Eastern Snow Conference*, 30, 1974.

Baumgartner, M.F., J. Marinec, and K. Seidel, Large-area deterministic simulation of natural runoff from snowmelt basins on Landsat MSS data, *IEEE Transactions of the Geoscience and Remote Sensing Symposium*, **GE-24**(6), 1013, 1986.

Blöschl, G., Scaling issues in snow hydrology, *Hydrological Processes*, **13**, 2149-2175, 1999.

Buttle, J.M., and J.J. McDonnell, Modelling the areal depletion of snowcover in a forested catchment. *Journal of Hydrology*, **90**, 43, 1987.

Carroll, S.S., and T.R. Carroll, Increasing the precision of snow water equivalent estimates obtained from spatial modeling of airborne and ground-based snow data, *Proceedings of the 61st Western Snow Conference, 50th Eastern Snow Conference*, 1993.

Carroll, T.R., D.W. Cline, G. Fall, A. Nilsson, L.Li, and A. Rost, NOHRSC Operations and simulation of snow cover properties for the coterminous US, *Proceedings of the 69th Western Snow Conference*, 2001.

Cline, D.W., and T.R. Carroll, Inference of snow cover beneath obscuring clouds using optical remote sensing and a distributed snow energy and mass balance model, *Journal of Geophysical Research*, **104**(D16), 19,631-19,644, 1999.

Cline, D.W., R.C. Bales, and J. Dozier, Estimating the spatial distribution of snow in mountain basins using remote sensing and energy balance modeling, *Water Resources Research*, **34**(5), 1275-1285, 1998.

Colee, M. T., *A high-resolution distributed snowmelt model in an alpine catchment*, Unpublished M.A. Thesis, Department of Geography, University of California at Santa Barbara, 2000.

Daly, S. F., R. E. Davis, E. Ochs, and T. Pangburn, An approach to spatially distributed snow modeling of the Sacramento and San Joaquin Basins, California, *Hydrological Processes*, **14**(18), 3257-3271, 2000.

Dunne T., and L.B. Leopold, *Water in Environmental Planning*, W.H. Freeman and Company, New York, 1978.

Fassnacht, S.R., K.A. Dressler, and R.C. Bales, *in submission*, Geostatistical interpolation of point-measured snow water equivalent in the Colorado River Basin, *Water Resources Research*.

Ferguson, R.I., Magnitude and modelling of snowmelt runoff in the Cairngorm Mountains, Scotland, *Hydrological Sciences*, **29**, 49, 1984.

Ferguson, R.I., Parametric modelling of daily and seasonal snowmelt using snowpack water equivalent as well as snow covered area, *Modelling snowmelt-induced processes (Proceedings of the Budapest Symposium, July 1986)*, IAHS Publication **155**, 151, 1986.

Kumar, V.S, H. Haefner, and K. Seidel, Satellite snow cover mapping and snowmelt runoff modelling in Beas basin, *Snow Hydrology and Forests in High Alpine Areas (Proceedings of the Vienna Symposium, August 1991)*, IAHS Publication **205**, 1991.

Liston, G.E., Interrelationships among snow distribution, snowmelt, and snow cover depletion: implications for atmospheric, hydrologic, and ecologic modeling, *Journal of Applied Meteorology*, **38**, 1474-1487, 1998.

Molotch, N. P., S.R. Fassnacht, M.T. Colee, T. Bardsley, and R.C. Bales, A comparison of spatial statistical techniques for the development of a validation dataset for mesoscale modeling of snow water equivalent, *AGU Eos Transactions, Fall Meeting Supplement,* **82**(47), 2001.

Rango, A., Progress in developing an operational snowmelt-runoff forecast model with remote sensing input, *Nordic Hydrology*, **19**, 65, 1988.

Rango, A., and J. Martinec, Snow accumulation derived from modified depletion curves of snow coverage, *Hydrological Aspects of Alpine and High Mountain Areas (Proceedings of the Exeter Symposium, July 1982)*, IAHS Publication **138**, 83, 1982.

Rosenthal, W., *Automated snow mapping at subpixel resolution from NOAA-AVHRR data. Final report: Programs for estimating subpixel snow-covered area,* Technical Report, U.S. Army Cold Regions Research and Engineering Laboratory, Hanover, N.H., 35 pp, 1996.

Salt River Project, *SRP: SRP managed dams*, Salt River Project, Phoenix Arizona, URL: <*http://www.srpnet.com/newsroom/facts.asp*>, 2002.

Serreze, M.C., M.P. Clark, R.L. Armstrong, D.A. McGuiness, and R.S. Pulwarty, Characteristics of the western United States snowpack from snowpack telemetry (SNOTEL) data, *Water Resources Research*, **35**(7) 2145-2160, 1999.

Simpson, J.J., J.R. Stitt, and M. Sienko, Improved estimates of the areal extent of snow cover from AVHRR data, *Journal of Hydrology*, **204**(1-4), 1-23, 1998.

SW RESAC, *1995 Southwestern Snow Cover Mapping Product CD*, Southwest Regional Earth Science Applications Center, Department of Hydrology and Water Resources, University of Arizona, Tucson AZ, 2002a.

SW RESAC, *Western U.S. Ground-Based Interpolated Snow Water Equivalent - Level 0 CD*, Southwest Regional Earth Science Applications Center, Department of Hydrology and Water Resources, University of Arizona, Tucson AZ, 2002b.

Swamy, A.N., P. A. Brivio, Modelling runoff using optical satellite remote sensing data in a high mountainous alpine catchment of Italy, *Hydrological Processes*, **11**, 1475, 1997.

United States Census Bureau, *Population estimates - Census 2000*, URL: <*http://www.census.gov/*>, 2002.

Vermote, E.F., D. Tanre, J.L. Deuze, M. Herman, and J.J. Morcrette, Second simulation of the satellite signal in the solar spectrum. 6S: an overview, *IEEE Transactions Geoscience and Remote Sensing*, **35** (3), 675-686, 1997.

Zuzel, J.F., Cox, L.M., Relative importance of meteorological variables in snowmelt, *Water Resources Research,* **11**(1), 1975.